Supporting Material: Probing the Elasticity of DNA on Short Length Scales by Modeling Supercoiling under Tension

Robert Schöpflin, Hergen Brutzer, Oliver Müller, Ralf Seidel, Gero Wedemann

SUPPORTING DISCUSSION

Parameterization of the electrostatic potential

For the computation of the DNA-DNA electrostatic interactions DNA molecules were approximated by charged cylinders with radius R and a linear charge density of $\chi_{CR} \cdot \xi_{DNA}$ with ξ_{DNA} = 2e/0.34 nm being the nominal charge density of DNA (see also Supporting Methods below). We used a charge adaptation factor χ_{CR} = 0.42 accounting for the lower effective charge density due to the highly structured nature of DNA and non-continuous counter ion density and a DNA radius R = 1.2 nm throughout all simulations. This parameter set was introduced by Maffeo et al. (1). It was found to quantitatively describe the postbuckling slopes and torques in simple theoretical models and Monte Carlo simulations of DNA supercoiling experiments under tension. In addition it was confirmed by all-atom molecular dynamics simulations (1). The particular value of χ_{CR} was found to be critical with slight variations failing to describe the experimental data. More recently, R = 1.0 nm and χ_{CR} = 1 was also reported to describe the postbuckling parameters with the full DNA charge considered to be a "standard" value (2). It was hypothesized that the low charge density used by Maffeo et al. is compensated by the larger radius. However, as demonstrated in Fig. S3, R = 1.0 nm and χ_{CR} = 1 provide ~1.7-fold increased interaction energies compared to Maffeo et al. (1). For our simulations presented, such large interaction energies significantly overestimate the postbuckling parameters and can therefore not be applied. We attribute the apparent success of the parameter set with R = 1.0 nm and χ_{CR} = 1 (2) to the following points: (i) the usage of a relative extension factor (which, however, is not necessary when comparing theoretical models with simulations (1)), (ii) the approximation of the superhelix by a straight, non-helical conformation and (iii) the residual but significant overestimation of the postbuckling slopes and torques with this parameter set. Points i (discussed in ref. (1)) and ii (2) both lower the initially overestimated postbuckling slopes and torques. There is also no reason to assume a "standard" value with χ_{CR} = 1 for the charge of DNA cylinder models. As shown with all-atom simulations (1) large part of the counterions are already located within the DNA grooves. Thus, the choice of any cylinder radius with an associated cylinder charge is anyway quite arbitrary.

Choice of the torsion modulus

The value for the torsion modulus applied in the simulations critically influences the position of the buckling point. We found that a torsion modulus of 90 nm×k_BT best reproduces the experimentally determined buckling point position (Fig. 3, main text), while applying 100 nm×k_BT leads to significant deviations (1). A torsion modulus of 90 nm×k_BT is in agreement

with recent measurements of Mosconi et al. (3), where a value of 94 nm×k_BT was found, of Lipfert et al. (4), which reported values of 88 and 95 nm×k_BT, of Obertrass et al. (5), where a value of 96 nm×k_BT was found, and Kauert et al. (6), that provide a value of 97 nm×k_BT. The slight deviations among the reported values may partially be caused by the interpolation that is used to estimate the DNA torsion modulus from the experimentally measured apparent torsional rigidities that are force dependent due to DNA bending fluctuations (4).
We verified that the apparent torsional rigidities extracted from our simulations exhibit the theoretically expected force dependence (Fig. S2). According to ref. (7) the dependence of the apparent torsional rigidity on the pulling force F can be approximated in first order by:

$$C_S = C\left[1 - \frac{C}{4p \times k_BT}\left(\frac{k_BT}{p \times F}\right)^{1/2}\right] \quad \text{(S1)}$$

where C denotes the nominal torsion modulus and p the bending persistence length. We determined the apparent torsional rigidity in the simulations from linear fits of the torque during twisting prior buckling (Fig. 1, main text). A comparison with the theoretical prediction reveal an almost quantitative agreement with data from simulations using WLC bending and 2.5 nm segments at forces ≥ 1 pN (Fig. S2). Simulations using 5 nm segments show to be slightly higher (by 1.7 nm×k_BT), while reproducing the overall shape of the curve.
We also verified that the simulations with a torsion modulus of 90 nm×k_BT reproduce the experimentally determined values for the postbuckling slopes over a large range of stretching forces and salt concentrations (Fig. S4 *a*). Within error the postbuckling slopes and torques obtained from the simulations (Fig. S4) agree also quantitatively with previous simulations using a torsion modulus of 100 nm×k_BT. The latter value was originally applied to reproduce the experimental postbuckling parameters (1). The independence of the postbuckling slopes and torques from the torsion modulus is expected based on theoretical models (1).

Simulations with 2.5 nm DNA segments

Since we expect bending radii in the end-loop of the superhelix that are smaller than the DNA segment length in the simulations, we performed a selected set of simulations using 2.5 nm DNA segments in addition to the normally applied 5 nm segments. We determined the position of the buckling points N_b and the length jumps (see Fig. 3, main text) as well as the postbuckling slopes and torques (Fig. S4). The obtained values reproduced the results obtained for 5 nm segments, suggesting that the conformational freedom of the DNA segments as well as the electrostatics of neighboring segments within the DNA chain are already well described by the larger segment size. Only when comparing the apparent torsional rigidities (see Fig. S2) the values appear increased by 1.7 nm×k_BT for a chain with 5 nm segments compared to a chain with 2.5 nm segments at forces ≥ 1 pN.

SUPPORTING METHODS

Coarse grained Monte Carlo simulations

The DNA is represented as a linear chain of straight segments. The majority of the simulations was performed with a chain of 5 nm segments with an overall length of 645 nm. A selected subset of simulations was performed with a chain of 2.5 nm segments to analyze discretization effects (see above). In the latter case the amount of segments was doubled to yield the same chain length. Each segment of the chain is defined by its position and a local coordinate system describing its spatial orientation. The elastic properties are modeled by standard harmonic potentials for stretching and torsion (8, 9). For DNA bending we used harmonic and non-harmonic potentials as indicated in the main text.

Throughout all simulations, the electrostatic interactions between two DNA segments i and j were determined using a Debye-Hückel potential for a point charge. The resulting interaction energy is then obtained by integration over the two line segments (1, 8, 10):

$$E_{ij}^{\text{Estat}} = l_{\text{B}} \cdot k_{\text{B}}T \cdot \xi^{*2} \int ds_i \int ds_j \frac{\exp(-r_{ij} / \lambda_{\text{D}})}{r_{ij}} \qquad \text{(S2)}$$

where l_{B} denotes the Bjerrum length in water and λ_{D} the Debye length. r_{ij} is the distance between the current positions s_i and s_j at the corresponding segments i and j. The effective charge density $\xi^* = \xi \cdot \chi_{\text{CR}} \cdot \chi_{\text{Rod}} \cdot \chi_{\text{PB}}$ is chosen such that the potential coincides with the exact solution of the Poisson-Boltzmann equation for charged cylinders with a radius of 1.2 nm and a charge density $\chi_{\text{CR}} \cdot \xi$, with ξ being the nominal charge of 2e/0.34 nm. The factor χ_{Rod} adapts the line charge to a homogeneously charged cylinder surface while χ_{PB} denotes the Poisson-Boltzmann adaptation of the Debye-Hückel potential.

Electrostatic interactions between neighboring segments were excluded and assumed to be comprised in the persistence length of the DNA. In order to save computation time, the values of the double integral of Eq. S2 were pre-tabulated for each applied ionic strength. The distance between the segments and their spatial orientation to each other are the parameters of the table. During the simulation the values of the table were interpolated linearly. Additional potentials were used to model the configuration of the magnetic tweezers experiments (1). The stretching of the DNA is implemented by the following potential (1):

$$E_{\text{Pull}} = \alpha_{\text{tether}} \cdot d^2 - F \cdot z \qquad \text{(S3)}$$

where the first term describes the tethering of the chain to a surface. d is the displacement of the first segment to its origin and α_{tether} a factor scaling the strength of the attachment. The second term models the stretching of the chain by the magnetic bead with the force F and the extension of the chain z. The movements of the chain were restricted by the impenetrable

attachment surface and the excluded volume of a sphere with a radius of 400 nm representing the volume of the magnetic bead. Both excluded volumes were realized by soft-core potentials. Prior to every simulation the chain was initialized as a straight, twisted chain. Additional segments with a fixed local coordinate system were used at both ends of the chain to prevent a free rotation of the chain ends. These capping segments were only considered in terms of their bending and twisting energy contribution.

Parameter	Value	
Stretching modulus	1100 pN	(11)
Torsion modulus	90 nm×k_BT	
Bending modulus (WLC)	50 nm×k_BT	(12)
LSEC parameter α	6.4	
Tether modulus	5530 pN / nm	
Temperature	293.0 K	
Number of segments	129 (258)	
Segment length	5 nm (2.5 nm)	

TABLE S1: Parameters used in the MC simulations. The elastic modulus for stretching and WLC bending were taken from literature as indicated.

Simulation procedure

An ensemble of configurations, representing thermal equilibrium distribution was generated using pivot, rotation (13, 14) and crankshaft moves (15, 16) as well as segment length variation (17). All simulations were performed at a temperature of 293.0 K. An overview of the simulation parameters is given in Tab. S1. The MC moves allow segments to cross each other, which can produce knotted configurations (15) or changes of the linking number *Lk* of the chain. To prevent such non-physical moves, the configuration was checked periodically (1) using a knot-finding algorithm (18) while *Lk* was verified using the condition $Lk = Tw + Wr$. The twist *Tw* can directly be derived from the simulation model while the writhe *Wr* was computed according to ref. (19). Every simulation run was carried out with $6 \cdot 10^7$ steps, and repeated at least five times for the analysis of the buckling transition. The first $2 \cdot 10^7$ steps were omitted to ensure system equilibration. To measure the number of uncorrelated configurations we determined the correlation times from the autocorrelation function as described in ref. (9) for the energy, the average twist and the *z*-position of the middle segment. The largest measured correlation length was $4.8 \cdot 10^4$ steps. Configurations separated more than two times the correlation length can be considered as statistically independent (20). Thus, we considered only every 10^5 simulation steps for analysis, yielding 400 uncorrelated samples from every simulation run and 2000 for all five reiterations.

Linear sub-elastic chain model for 5 nm segments

The majority of Monte Carlo simulations was performed with 5 nm segments. To adapt the bending potential, that was originally developed for 2.5 nm segments (Eq. 2, main text), the angular distributions for two consecutive 2.5 nm segments need to be convoluted (21):

$$p_{\mathrm{LSEC}}^{2.5\mathrm{nm}}(\theta) = \frac{\alpha}{2}\mathrm{e}^{-\alpha|\theta|} \tag{S4}$$

$$p_{\mathrm{LSEC}}^{5\mathrm{nm}}(\theta) = \int_{-\infty}^{\infty} \frac{\alpha^2}{4}\mathrm{e}^{-\alpha|\tau|} \cdot \mathrm{e}^{-\alpha|\theta-\tau|}\, d\tau \tag{S5}$$

The integral can be simplified to:

$$p_{\mathrm{LSEC}}^{5\mathrm{nm}}(\theta) = \frac{1}{4}\mathrm{e}^{-\alpha\theta}\alpha + \frac{1}{4}\mathrm{e}^{-\alpha\theta}\alpha^2\theta \tag{S6}$$

Presuming θ to be non-negative and $\alpha > 0$, Eq. S6 can be further simplified to:

$$p_{\mathrm{LSEC}}^{5\mathrm{nm}}(\theta) = \frac{1}{4}\mathrm{e}^{-\alpha\theta}\alpha(1+\alpha\theta) \tag{S7}$$

The bending potential for 5 nm segments was derived from the angular distribution:

$$E_{\mathrm{LSEC}}^{5\mathrm{nm}} = k_{\mathrm{B}}T(\ln(4) + \alpha|\theta| - \ln(\alpha) - \ln(1+\alpha|\theta|)) \tag{S8}$$

We omitted all constant terms (see Eq. 5, main text), since the Metropolis Monte Carlo algorithm is based solely on energy differences.

SUPPORTING FIGURES

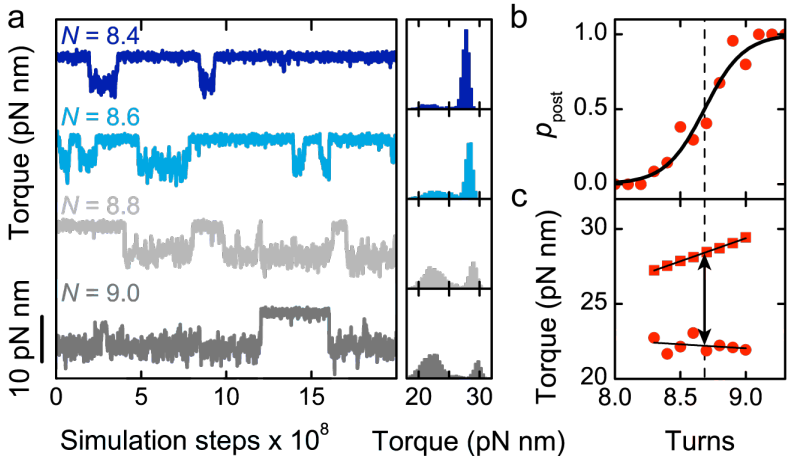

FIGURE S1: Analysis of the torque jump upon buckling from simulations carried out at 3.0 pN force and 170 mM monovalent salt, corresponding to the analysis of the length jump in Fig. 2, main text. (*a*) DNA torque over simulation time at different numbers of turns N with corresponding histograms (shown on the right). Transitions between the pre- and the post-buckling state can be clearly seen. The results of five independent simulations were concatenated to improve the number of events. (*b*) Occupancy of the postbuckling state as function of the applied turns obtained from the histograms shown in (*a*). The solid line is a fit according to Eq. 3, main text. The dashed line indicates the buckling position N_b at which the DNA has the same probability to be in the pre- and the postbuckling state. (*c*) Mean DNA torque of the pre- and the postbuckling state (squares and circles, respectively) as function of turns obtained from the histograms shown in (*a*). The arrow indicates the size of the torque jump at the buckling position as obtained from linearly interpolating the DNA lengths (solid lines).

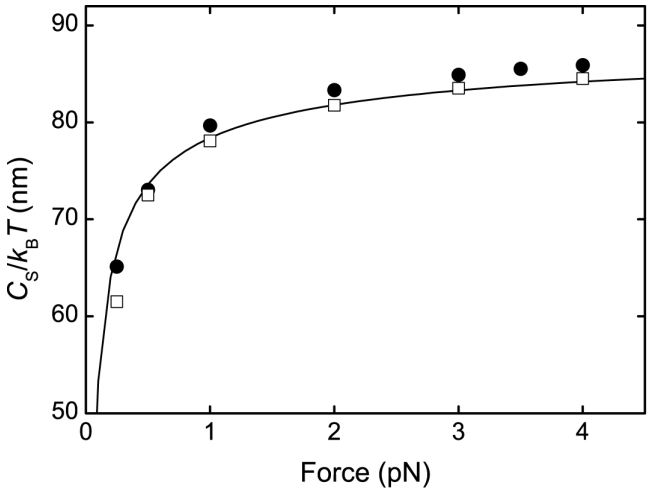

FIGURE S2: Apparent torsion modulus as function of force derived from simulations with WLC bending for a bending persistence length p = 50 nm and a torsion modulus C = 90 nm×k_BT at 320 mM monovalent ions for 5 nm segments (filled circles) and 2.5 nm segments (open squares). The apparent torsion modulus was obtained from linear fits of the torque data prior buckling (see Fig. 1 *c*, main text). The theoretical prediction by Moroz and Nelson (Eq. S1) is shown as a solid line.

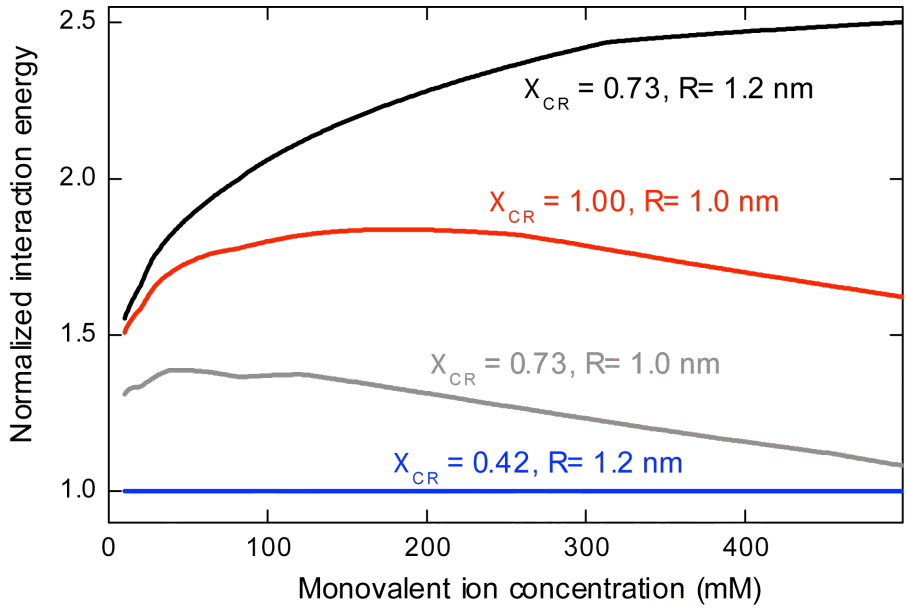

FIGURE S3: Dependence of the interaction energies of two parallel DNA molecules on the monovalent ion concentration for different model parameters. DNA molecules were approximated by charged cylinders with radius R and a linear charge density of $\chi_{CR} \cdot \xi_{DNA}$ with ξ_{DNA} = 2e/0.34 nm being the nominal charge density of DNA. Interaction energies for different values of R and χ_{CR} were calculated as previously described (see above (1, 10, 22)). Interaction energies were normalized by division with the values obtained using R = 1.2 nm and χ_{CR} = 0.42. In addition to the parameter set R = 1.0 nm and χ_{CR} = 1.00 (2) (see discussion above), we also show interaction energies for the parameter set originally introduced by Stigter and coworkers (10, 23) with R = 1.2 nm and χ_{CR} = 0.73 as well as for R = 1.0 nm and χ_{CR} = 0.73. Even in the latter case the interaction energies are significantly overestimated compared to R = 1.2 nm and χ_{CR} = 0.42. Since the decay of the electrostatic potential with distance from the DNA is the same for all parameter sets, the ratios between the interaction energies for different parameterizations and thus the normalized interaction energies are independent of distance.

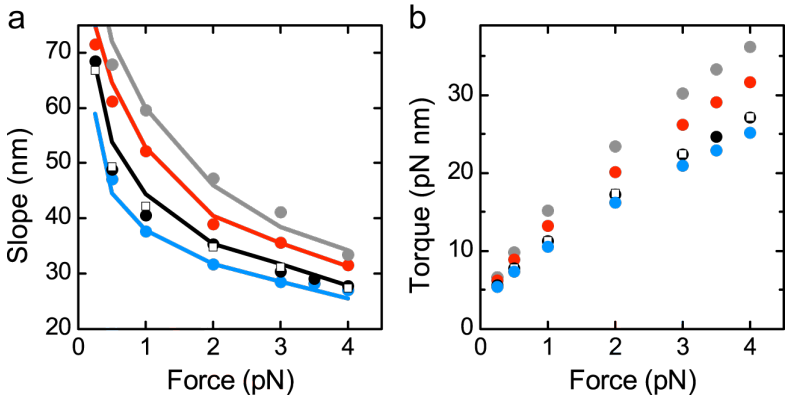

FIGURE S4: Postbuckling parameters from simulations for a torsional rigidity of 90 nm×k_BT using 5 or 2.5 nm DNA segments. (*a*) Slopes corresponding to the linear DNA length decrease per turn in the postbuckling phase as function of the applied stretching force for 30, 60, 170 and 320 mM monovalent salt (gray, red, black and blue, respectively). Lines represent data from magnetic tweezers experiments (1) while results from WLC simulations with 5 nm DNA segments are depicted as filled circles. Simulations for 170 mM monovalent ions using 2.5 nm segments are shown as open squares. (*b*) Torque in the postbuckling phase, corresponding to the WLC simulations in (*a*).

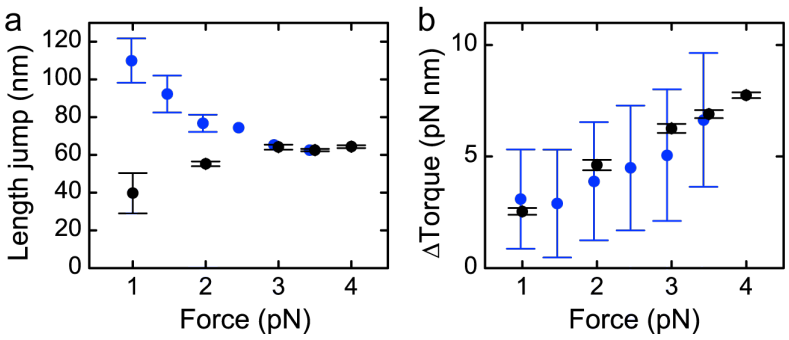

FIGURE S5: Force dependence of the length jump (*a*) and the torque jump (*b*) compared to measurements using optical tweezers (24). Data from WLC simulation for 170 mM monovalent salt are depicted as black dots while data from optical tweezers experiments at 150 mM NaCl DNA template length of 2.2 kbp are shown as blue dots. The force dependence of the length jump from simulations is in better agreement with magnetic tweezers measurements (Fig. 3 *b*, main text), which found a nearly constant jump size with decreasing force. The strongly increasing jump sizes at low forces found in the optical tweezers measurements are probably due to a different way of analyzing this data. Jump sizes were in this case obtained from fits of the supercoiling curves (24) instead of analyzing the distributions of pre- and postbuckling state as done in the present study (see Figs. 2, main text and S1). Noticeably, the torque jump obtained from the simulations agrees within errors with the experimental results, though more precise measurements are still required to more stringently validate this data.

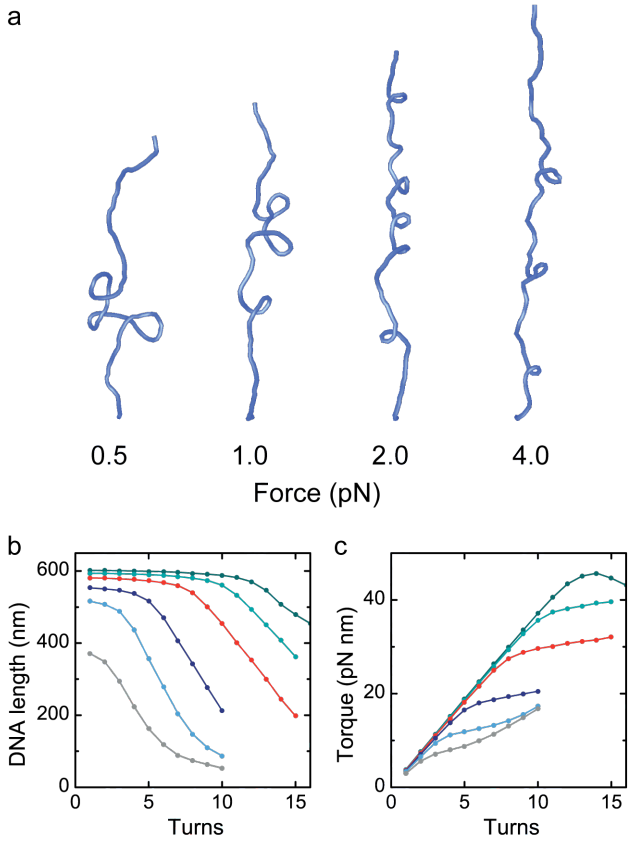

FIGURE S6: Simulation of DNA supercoiling under tension with WLC bending elasticity at low ionic strength (10 mM Na^+) using a torsional rigidity of 100 nm×k_BT. The energy barrier between the formation energy of the initial loop (E_{loop}) and the formation energy of the plectonemic superhelix (E_{helix}) disappears due to the reduced screening of the electrostatic repulsion at low ionic strength. As a consequence the buckling disappears while multiple initial loops are formed instead of an extended plectonemic superhelix. (a) Representative snapshots from the simulations at different stretching forces. The radius of the visualized DNA was doubled to improve clarity. (b) DNA length versus applied turns at different forces (0.25 pN to 4.0 pN, colors as in Fig. 1*b*). (c) Torque values for the simulations shown in (b).

SUPPORTING REFERENCES

1. Maffeo, C., R. Schöpflin, H. Brutzer, R. Stehr, A. Aksimentiev, et al. 2010. DNA-DNA Interactions in Tight Supercoils Are Described by a Small Effective Charge Density. Phys. Rev. Lett. 105: 158101.

2. Neukirch, S., and J.F. Marko. 2011. Analytical Description of Extension, Torque, and Supercoiling Radius of a Stretched Twisted DNA. Phys. Rev. Lett. 106: 138104.

3. Mosconi, F., J.F. Allemand, D. Bensimon, and V. Croquette. 2009. Measurement of the Torque on a Single Stretched and Twisted DNA Using Magnetic Tweezers. Phys. Rev. Lett. 102: 078301.

4. Lipfert, J., M. Wiggin, J.W.J. Kerssemakers, F. Pedaci, and N.H. Dekker. 2011. Freely orbiting magnetic tweezers to directly monitor changes in the twist of nucleic acids. Nat. Commun. 2: 439.

5. Oberstrass, F.C., L.E. Fernandes, and Z. Bryant. 2012. Torque measurements reveal sequence-specific cooperative transitions in supercoiled DNA. Proc. Natl. Acad. Sci. USA. 109: 6106–6111.

6. Kauert, D.J., T. Kurth, T. Liedl, and R. Seidel. 2011. Direct Mechanical Measurements Reveal the Material Properties of Three-Dimensional DNA Origami. Nano Lett. 11: 5558–5563.

7. Moroz, J.D., and P. Nelson. 1998. Entropic Elasticity of Twist-Storing Polymers. Macromolecules. 31: 6333–6347.

8. Klenin, K., H. Merlitz, and J. Langowski. 1998. A Brownian Dynamics Program for the Simulation of Linear and Circular DNA and Other Wormlike Chain Polyelectrolytes. Biophys. J. 74: 780–788.

9. Wedemann, G., and J. Langowski. 2002. Computer simulation of the 30-nanometer chromatin fiber. Biophys. J. 82: 2847–2859.

10. Stigter, D. 1977. Interactions of highly charged colloidal cylinders with applications to double−stranded DNA. Biopolymers. 16: 1435–1448.

11. Wang, M.D., H. Yin, R. Landick, J. Gelles, and S.M. Block. 1997. Stretching DNA with optical tweezers. Biophys. J. 72: 1335–1346.

12. Bloomfield, V.A., D.M. Crothers, and I. Tinoco. 2000. Nucleic acids: structures, properties, and functions. University Science Books.

13. Metropolis, N., A.W. Rosenbluth, M.N. Rosenbluth, A.H. Teller, and E. Teller. 1953. Equation of State Calculations by Fast Computing Machines. J. Chem. Phys. 21: 1087–1092.

14. Baumgärtner, A., and K. Binder. 1979. Monte Carlo studies on the freely jointed polymer chain with excluded volume interaction. J. Chem. Phys. 71: 2541.

15. Vologodskii, A.V., and J.F. Marko. 1997. Extension of torsionally stressed DNA by external force. Biophys. J. 73: 123–132.

16. Arya, G., and T. Schlick. 2007. Efficient global biopolymer sampling with end-transfer configurational bias Monte Carlo. J. Chem. Phys. 126: 044107–12.

17. Binder, K. 1995. Monte Carlo and Molecular Dynamics Simulations in Polymer Science. Oxford University Press.

18. Khatib, F., M.T. Weirauch, and C.A. Rohl. 2006. Rapid knot detection and application to protein structure prediction. Bioinformatics. 22: e252–e259.

19. Klenin, K., and J. Langowski. 2000. Computation of writhe in modeling of supercoiled DNA. Biopolymers. 54: 307–317.

20. Sokal, A.D. 1996. Monte Carlo methods in statistical mechanics: foundations and new algorithms. In: DeWitt-Morette C, P Cartier, A Folacci, editors. Functional Integration: Basics and Applications. Proceedings of the NATO ASI B-361. Cargese (France): .

21. Wiggins, P.A., T. van der Heijden, F. Moreno-Herrero, A. Spakowitz, R. Phillips, et al. 2006. High flexibility of DNA on short length scales probed by atomic force microscopy. Nat. Nanotechnol. 1: 137–141.

22. Brenner, S.L., and V.A. Parsegian. 1974. A Physical Method for Deriving the Electrostatic Interaction between Rod-Like Polyions at All Mutual Angles. Biophys. J. 14: 327–334.

23. Schellman, J.A., and D. Stigter. 1977. Electrical double layer, zeta potential, and electrophoretic charge of double–stranded DNA. Biopolymers. 16: 1415–1434.

24. Daniels, B.C., S. Forth, M.Y. Sheinin, M.D. Wang, and J.P. Sethna. 2009. Discontinuities at the DNA supercoiling transition. Phys. Rev. E. 80: 040901.